Electronic Supporting Information

Liberation of carbon monoxide from formic acid mediated by molybdenum oxyanions.

Howard Z. Ma,[a] Allan J. Canty [b] and Richard A. J. O'Hair *[a]

(a) School of Chemistry and Bio21 Molecular Science and Biotechnology Institute, University of Melbourne, 30 Flemington Rd, Parkville, Victoria 3010, Australia. Fax: (+) 61 3 9347 8124; E-mail: rohair@unimelb.edu.au

(b) School of Natural Sciences – Chemistry, University of Tasmania, Private Bag 75, Hobart, Tasmania, 7001, Australia.

Crystallography

Intensity data for $(TBA)_2[Mo_2O_7]$ was collected on a Rigaku XtalLAB Synergy at 100.0(1) K. The temperature was maintained using an Oxford Cryostream cooling device. The structures were solved by direct methods and difference Fourier synthesis.[1] Thermal ellipsoid plot were generated using the program Mercury [2] integrated within the WINGX [3] suite of programs.

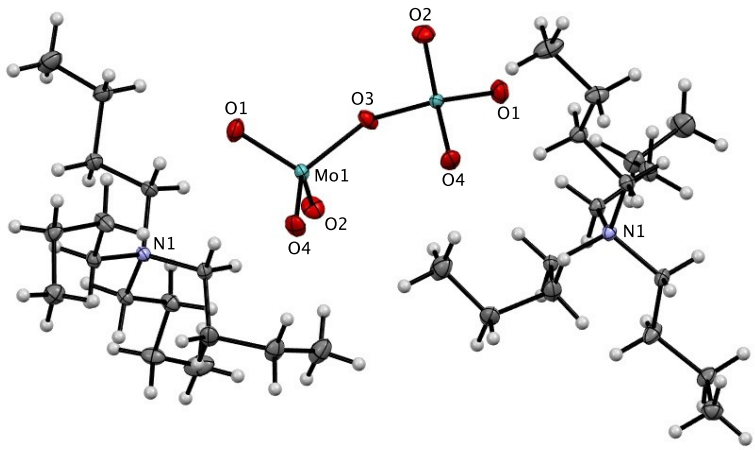

Fig. S1 Solid-state structure of $(TBA)_2[Mo_2O_7]$. This structure is similar to that reported in ref 20.

Crystal data for $(TBA)_2[Mo_2O_7]$. $C_{32}H_{72}Mo_2N_2O$, M = 788.79, T = 100.0 K, λ = 0.71073 Å, Monoclinic, space group I2/a, a = 17.1743(3)) b = 13.7314(2), c =18.0806(3) Å, β = 114.029(2)° V = 3894.38(12) Å^3, Z = 4, Z' = 0.5, D_c = 1.345 mg M^{-3} μ(Mo-Kα) 0.686 mm^{-1}, F(000) = 1672 crystal size 0.41 x 0.38 x 0.12 mm^3, 30977 reflections measured θ_{max} = 41.04°,

12327 independent reflections [R(int) = 0.029], the final R was 0.0295 [I > 2s(I), 10255 data] and *w*R(F^2) was 0.0702 (all data), GOF 1.061. CCDC deposit code 2291910.

Table S1: Selected distances (Å), angles (°) and dihedral angles (°) for $(TBA)_2[Mo_2O_7]$

O(1)-Mo(1)	1.7321(7)	O(2)-Mo(1)	1.7357(8)
O(3)-Mo(1)#1	1.8962(3)	O(3)-Mo(1)	1.9862(3)
O(4)-Mo(1)	1.7270(7)		
Mo(1)#1-O(3)-Mo(1)	148.56(6)	O(4)-Mo(1)-O(1)	108.62(4)
O(4)-Mo(1)-O(2)	110.35(4)	O(1)-Mo(1)-O(2)	108.89(4)
O(4)-Mo(1)-O(3)	109.79(4)	O(1)-Mo(1)-O(3)	109.52(3)
O(2)-Mo(1)-O(3)	109.65(3)		
Mo(1)#1-O(3)-Mo(1)-O(4)		7.43(3)	
Mo(1)#1-O(3)-Mo(1)-O(1)		126.61(3)	
Mo(1)#1-O(3)-Mo(1)-O(2)		-113.96(3)	

Symmetry transformations used to generate equivalent atoms: (#1 -x+1/2,y,-z+1)

Mass spectrometry

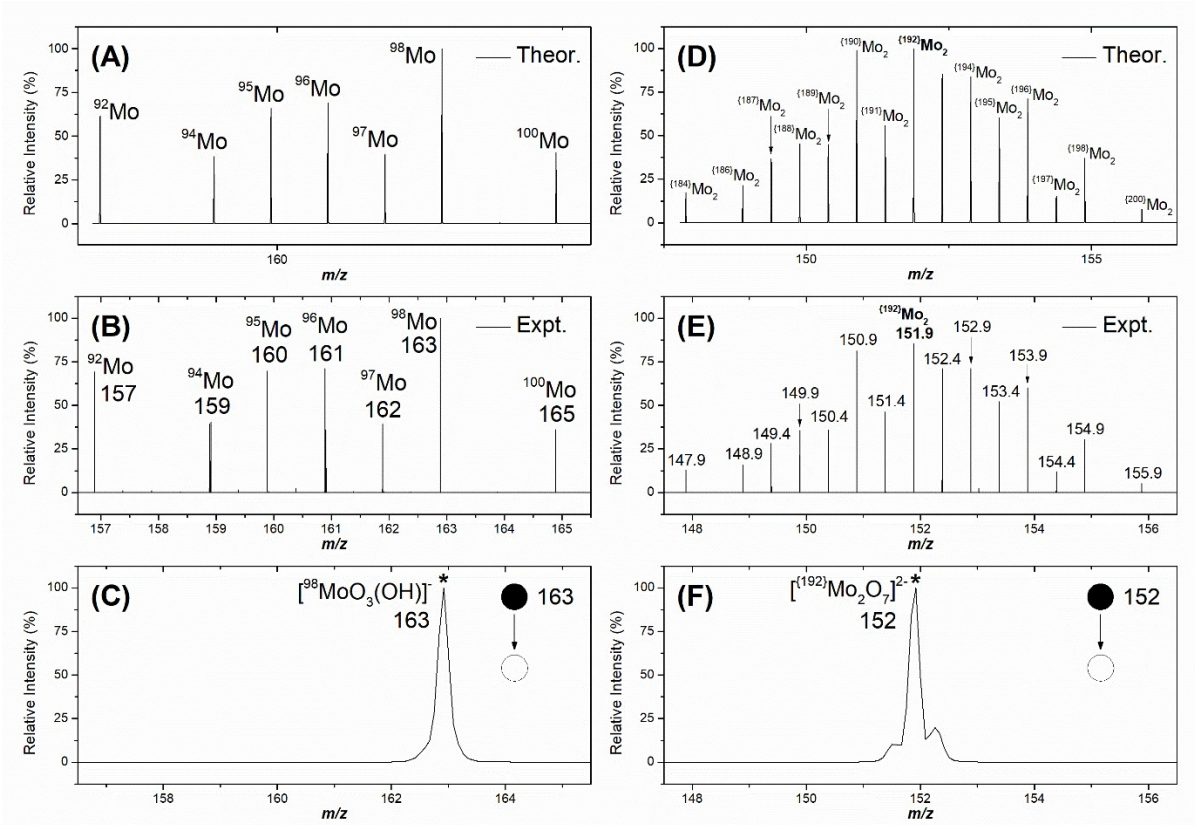

Fig. S2 (A) Theoretical isotope pattern of $[MoO_3(OH)]^-$; (B) Orbitrap experimental isotope pattern of the ion assigned as $[MoO_3(OH)]^-$; (C) Mass selection of a single peak at *m/z* 163 in the ion trap which corresponds to $[^{98}MoO_3(OH)]^-$; (D) Theoretical isotope pattern of $[Mo_2O_7]^{2-}$; (E) Orbitrap experimental isotope pattern of the ion assigned as $[Mo_2O_7]^{2-}$; Mass selection of a single peak at *m/z* 152 in the ion trap which corresponds to $[^{\{192\}}Mo_2O_7]^{2-}$.

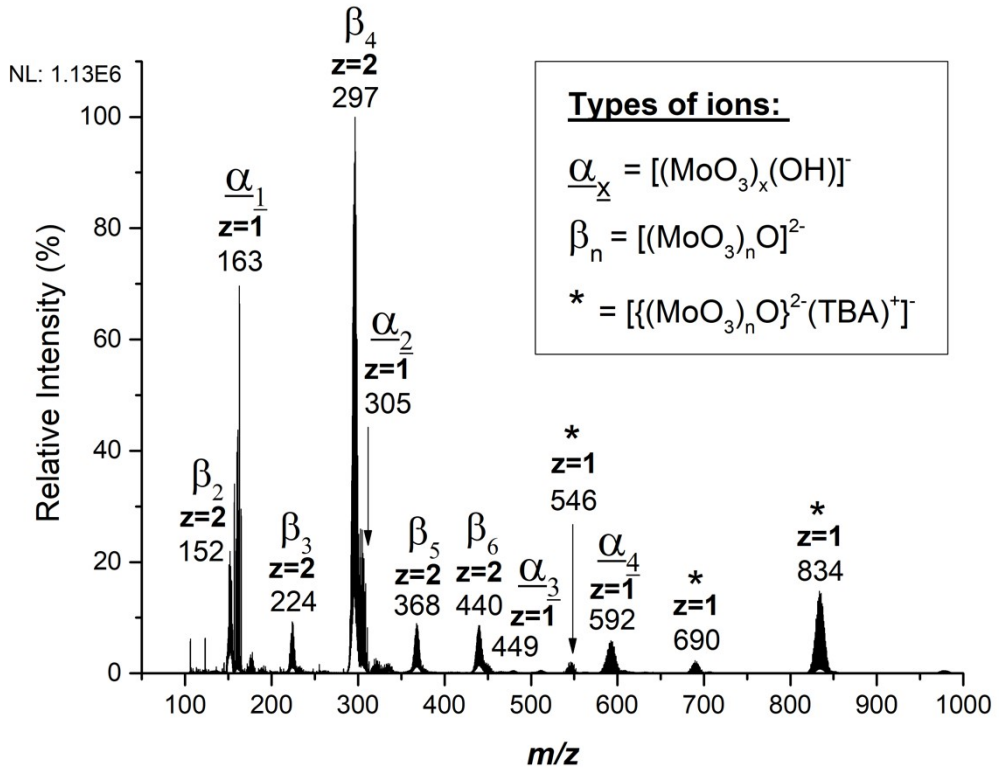

Fig. S3 Negative ion mode ion trap ESI-MS of $(TBA)_2[Mo_2O_7]$ in acetonitrile showing the formation of several molybdate oxyanions. α_x ions: $[(MoO_3)_1(OH)]^-$ (*m/z* 163); $[(MoO_3)_2(OH)]^-$ (*m/z* 305); $[(MoO_3)_3(OH)]^-$ (*m/z* 449); $[(MoO_3)_4(OH)]^-$ (*m/z* 593). β_n ions: $[(MoO_3)_2O]^{2-}$ (*m/z* 152); $[(MoO_3)_3O]^{2-}$ (*m/z* 224); $[(MoO_3)_4O]^{2-}$ (*m/z* 297); $[(MoO_3)_5O]^{2-}$ (*m/z* 368); $[(MoO_3)_6O]^{2-}$ (*m/z* 440). * ions: $[\{(MoO_3)_2O\}^{2-}(TBA)^+]^-$ (*m/z* 546); $[\{(MoO_3)_3O\}^{2-}(TBA)^+]^-$ (*m/z* 690); $[\{(MoO_3)_4O\}^{2-}(TBA)^+]^-$ (*m/z* 834). TBA = tetrabutylammonium, z represents the charge state of the anion.

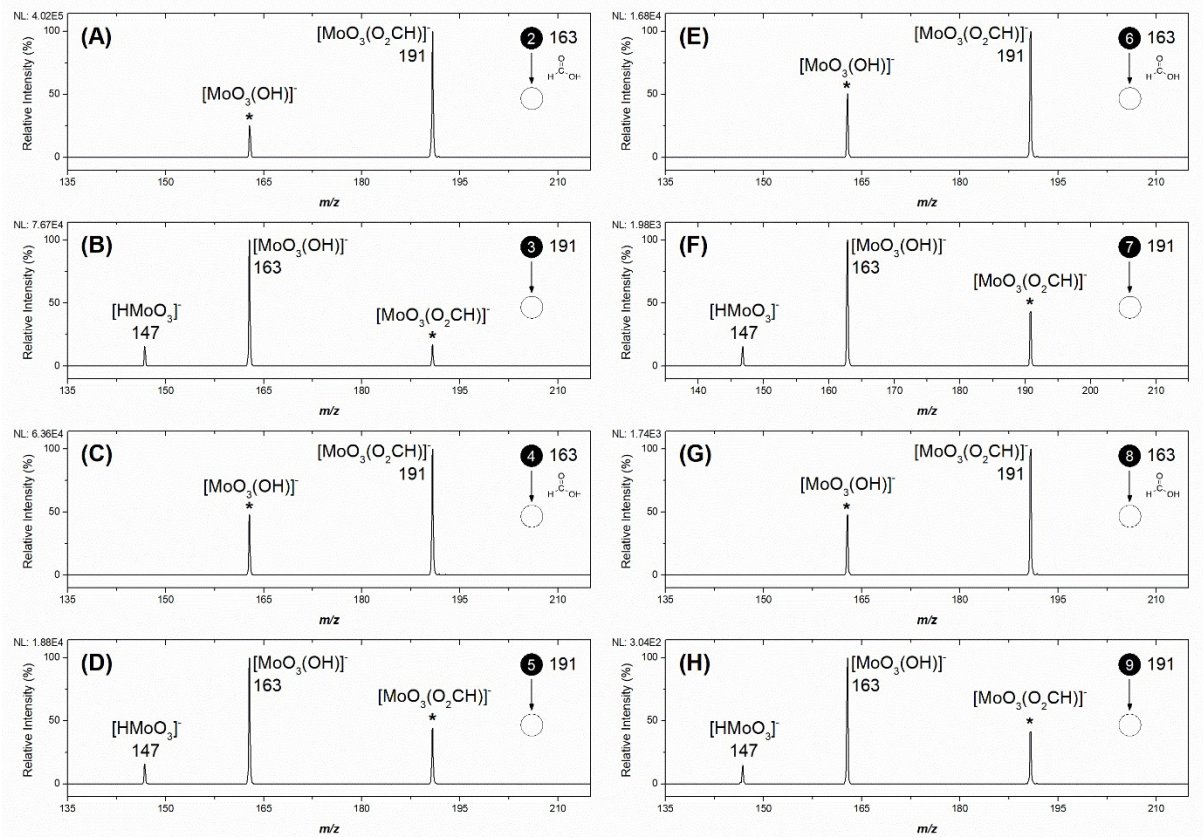

Fig. S4 Multistage mass spectrometry (MS^n) experiments demonstrating a two-step gas-phase catalytic cycle for the decomposition of formic acid (Scheme 1D). Ion-molecule reactions (IMR) of $[MoO_3(OH)]^-$ (*m/z* 163) with HCO_2H were obtained at the given activation times, collision-induced dissociation (CID) experiments on $[MoO_3(O_2CH)]^-$ (*m/z* 191) were obtained using a Q value of 0.25 and an activation time of 10 ms with the given Normalised Collision Energies (NCE): (A) MS^2 IMR (at 1300 ms); (B) MS^3 CID (NCE = 13%); (C) MS^4 IMR (at 1200 ms); (D) MS^5 CID (NCE = 12%); (E) MS^6 IMR (at 1200 ms); (F) MS^7 CID (NCE = 12%); (G) MS^8 IMR (at 1200 ms); (H) MS^9 CID (NCE = 12%). An asterisk (*) denotes the mass selected precursor ion.

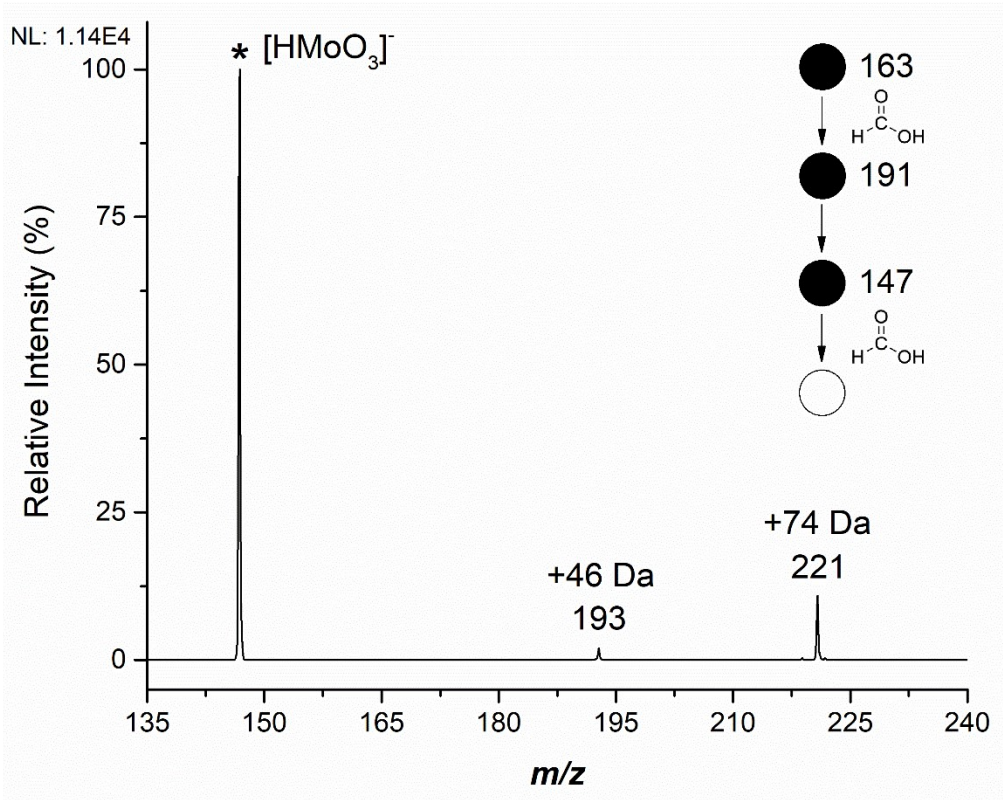

Fig. S5 MS^4 IMR experiment of $[HMoO_3]^-$ (*m/z* 147) with HCO_2H ($[HCO_2H]_{ion\ trap}$ = 9.2 × 10^9 molecules cm^{-3}) at an activation time of 10,000 ms. An asterisk (*) denotes the mass selected precursor ion.

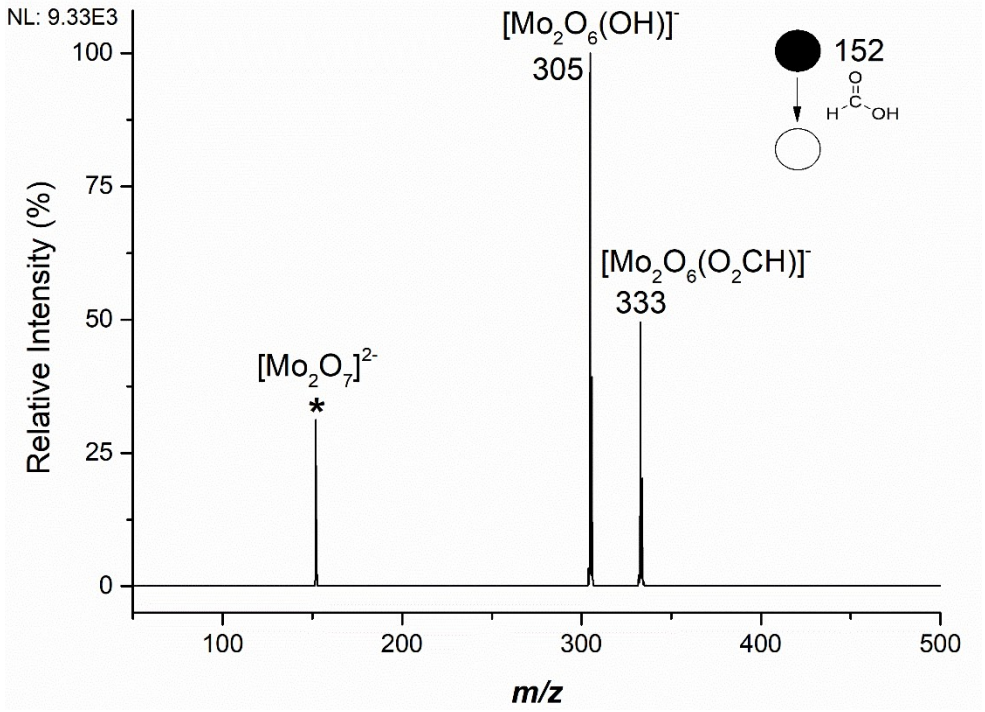

Fig. S6 MS^2 IMR on $[Mo_2O_7]^{2-}$ (*m/z* 152) with HCO_2H showing the formation of the primary product ion $[Mo_2O_6(OH)]^-$ (*m/z* 305) and the secondary product ion $[Mo_2O_6(O_2CH)]^-$ (*m/z* 333). The formate anion HCO_2^- (*m/z* 45), which is the other product ion formed upon protonation of $[Mo_2O_7]^{2-}$ by HCO_2H, is not experimentally observed due to the low mass cut-off of the ion trap.

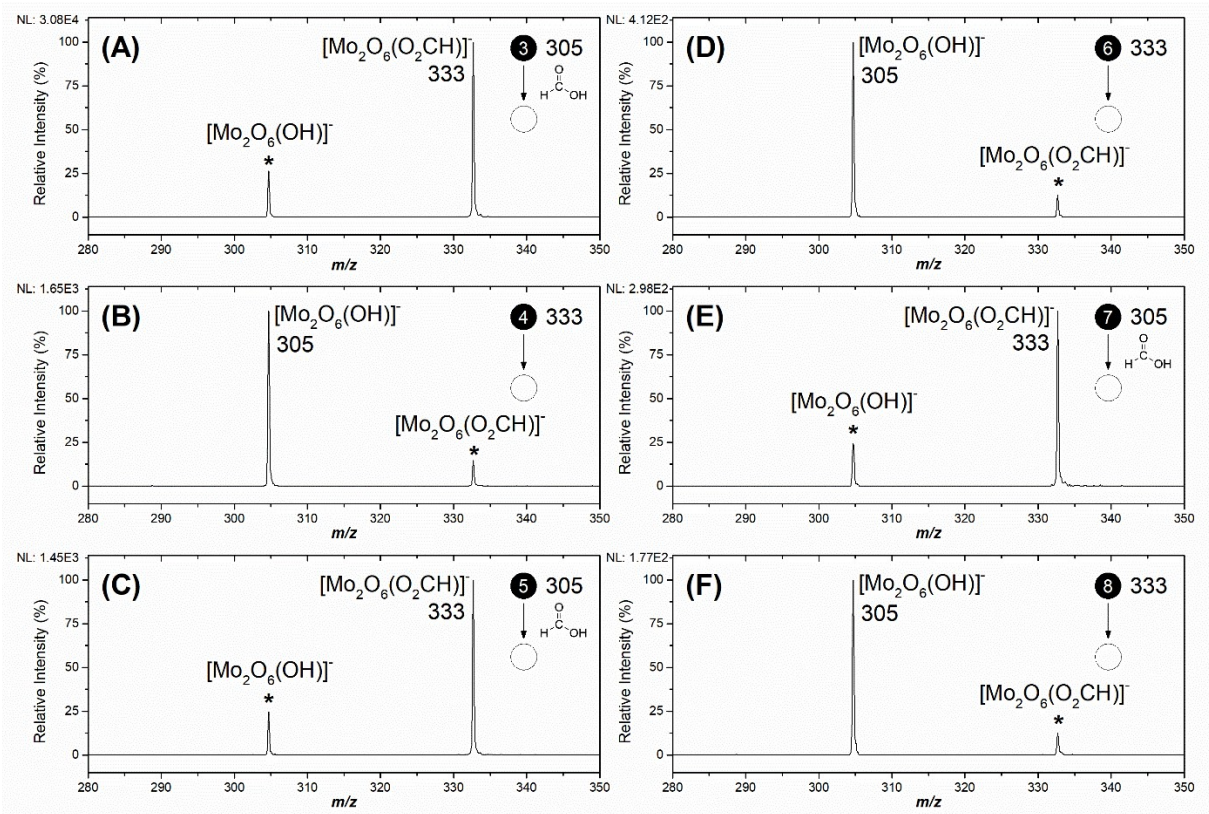

Fig. S7 Multistage mass spectrometry (MS^n) experiments on $[Mo_2O_6(O_2CH)]^-$ demonstrating a two-step gas-phase catalytic cycle for the selective decomposition of formic acid. Ion-molecule reactions (IMR) of $[Mo_2O_6(OH)]^-$ (*m/z* 305) with HCO_2H were obtained at the given activation times, collision-induced dissociation (CID) experiments on $[Mo_2O_6(O_2CH)]^-$ (*m/z* 333) were obtained using a Q value of 0.25 and an activation time of 10 ms with the given Normalised Collision Energies (NCE): (A) MS^3 IMR (at 200 ms); (B) MS^4 CID (NCE = 8%); (C) MS^5 IMR (at 200 ms); (D) MS^6 CID (NCE = 8%); (E) MS^7 IMR (at 200 ms); (F) MS^8 CID (NCE = 8%). An asterisk (*) denotes the mass selected precursor ion.

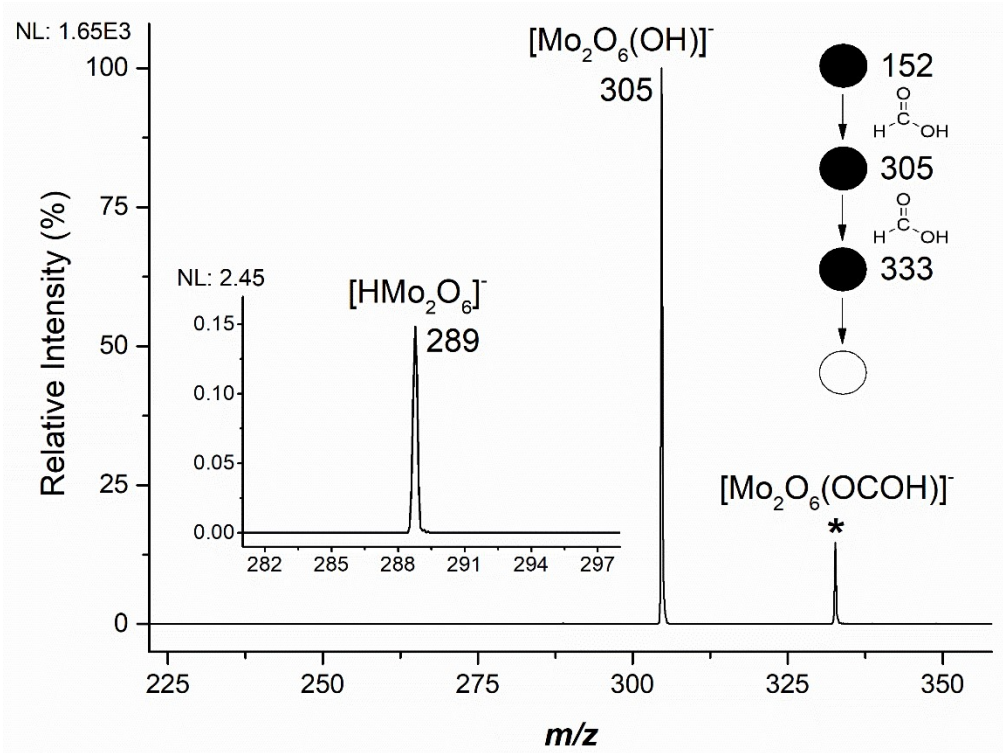

Fig. S8 MS^4 CID experiment of $[Mo_2O_6(O_2CH)]^-$ (m/z 333) illustrating decarbonylation, to produce $[Mo_2O_6(OH)]^-$ (*m/z* 305) as the major product ion, is preferred over decarboxylation to produce $[HMo_2O_6]^-$ (*m/z* 289) as a minor product ion. Spectrum obtained using a Q value of 0.25, an activation time of 10 ms and at an NCE of 8%. An asterisk (*) denotes the mass selected precursor ion.

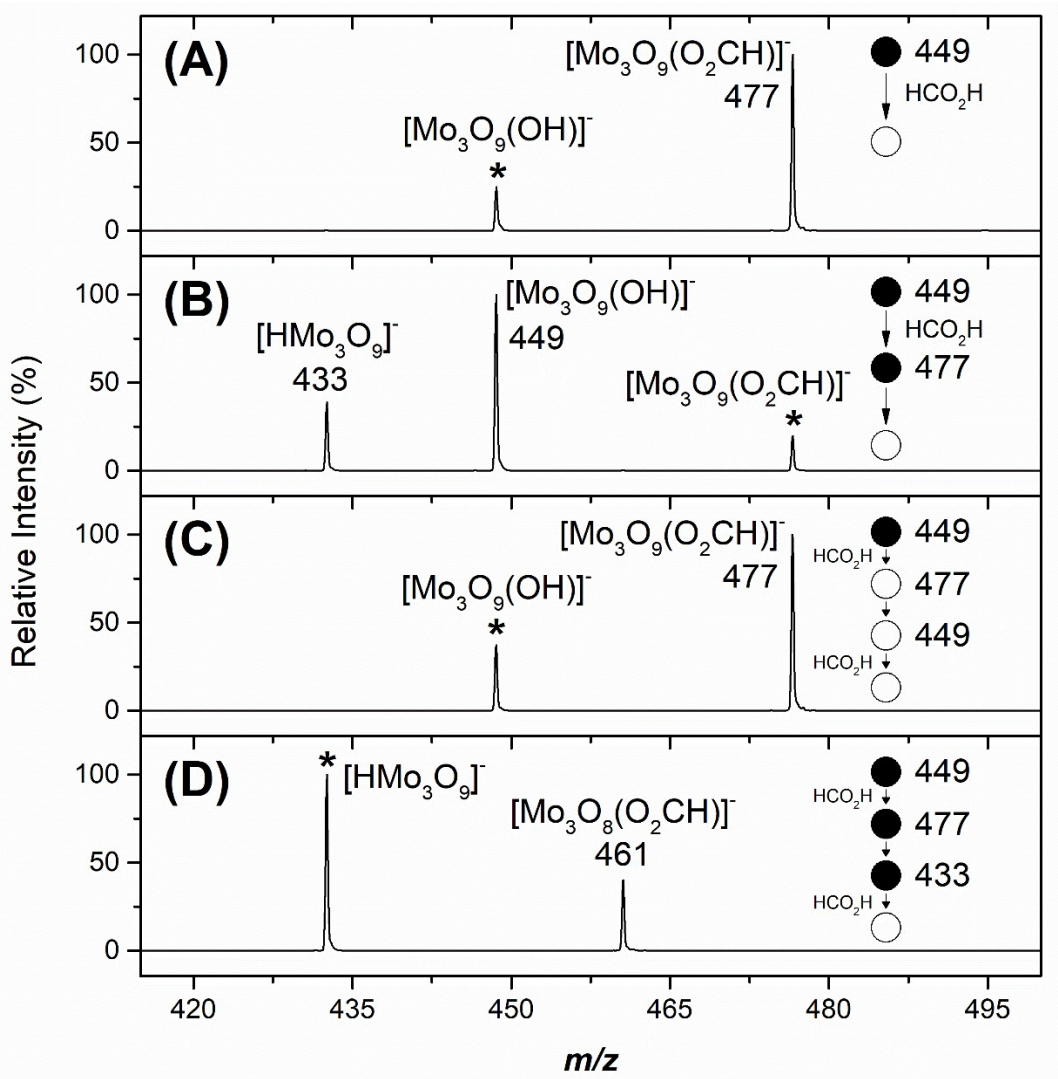

Fig. S9 Multistage mass spectrometry (MS^n) experiments on $[Mo_3O_9(O_2CH)]^-$ demonstrating a two-step gas-phase catalytic cycle for the decomposition of formic acid. (A) MS^2 IMR of $[Mo_3O_9(OH)]^-$ (*m/z* 449) with HCO_2H at an activation time of 300 ms; (B) MS^3 CID of $[Mo_3O_9(O_2CH)]^-$ (*m/z* 477) obtained using an activation Q of 0.25, an activation time of 10 ms and a Normalised Collision Energy (NCE) of 8.5%; (C) MS^4 IMR of $[Mo_3O_9(OH)]^-$ (*m/z* 449) with HCO_2H at an activation time of 200 ms; (D) MS^4 IMR of $[HMo_3O_9]^-$ (*m/z* 433) with HCO_2H at an activation time of 100 ms. An asterisk (*) denotes the mass selected precursor ion.

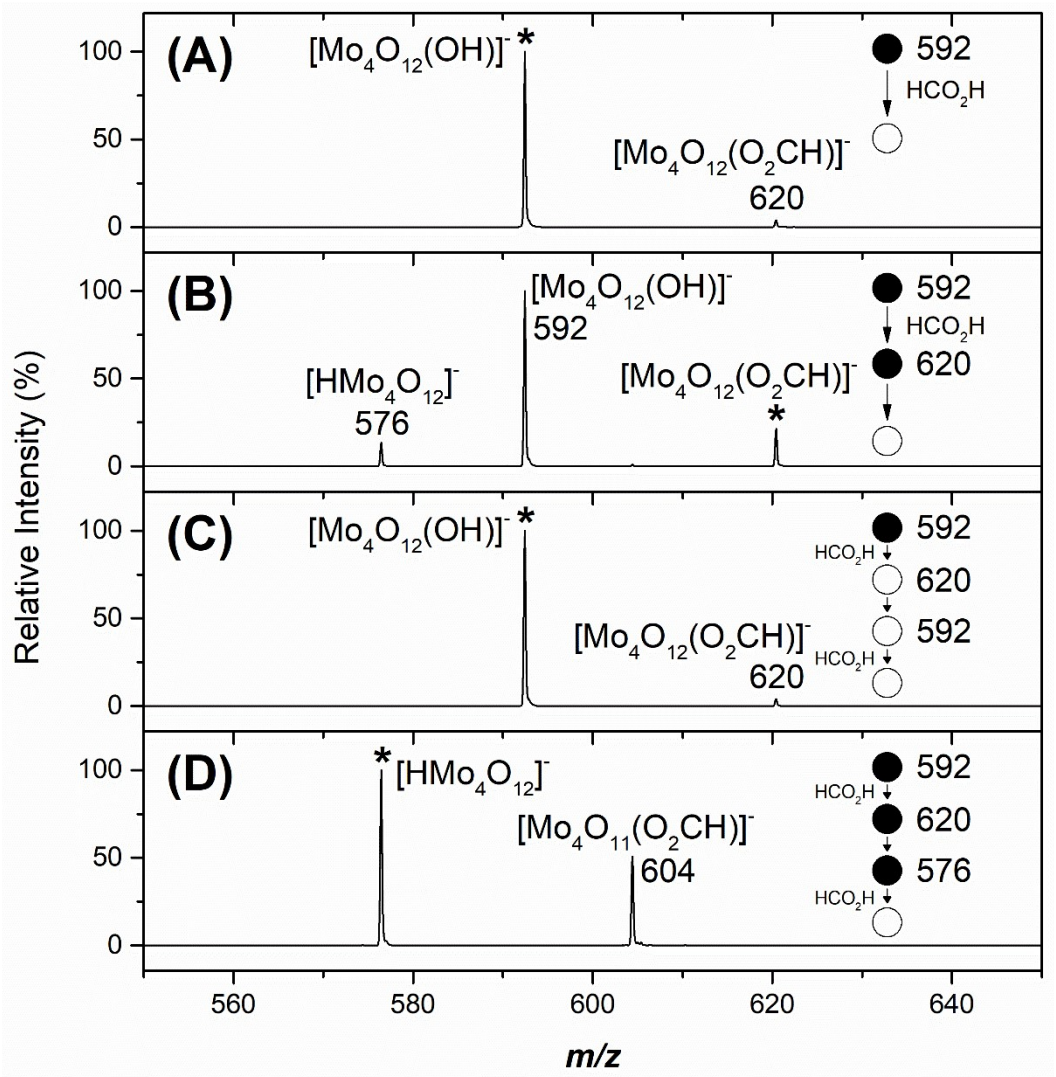

Fig. S10 Multistage mass spectrometry (MS^n) experiments on $[Mo_4O_{12}(O_2CH)]^-$ demonstrating a two-step gas-phase catalytic cycle for the decomposition of formic acid. (A) MS^2 IMR of $[Mo_4O_{12}(OH)]^-$ (*m/z* 592) with HCO_2H at an activation time of 5000 ms; (B) MS^3 CID of $[Mo_4O_{12}(O_2CH)]^-$ (*m/z* 620) obtained using an activation Q of 0.25, an activation time of 10 ms and a Normalised Collision Energy (NCE) of 7.5%; (C) MS^4 IMR of $[Mo_4O_{12}(OH)]^-$ (*m/z* 592) with HCO_2H at an activation time of 5000 ms; (D) MS^4 IMR of $[HMo_4O_{12}]^-$ (*m/z* 576) with HCO_2H at an activation time of 30 ms. An asterisk (*) denotes the mass selected precursor ion.

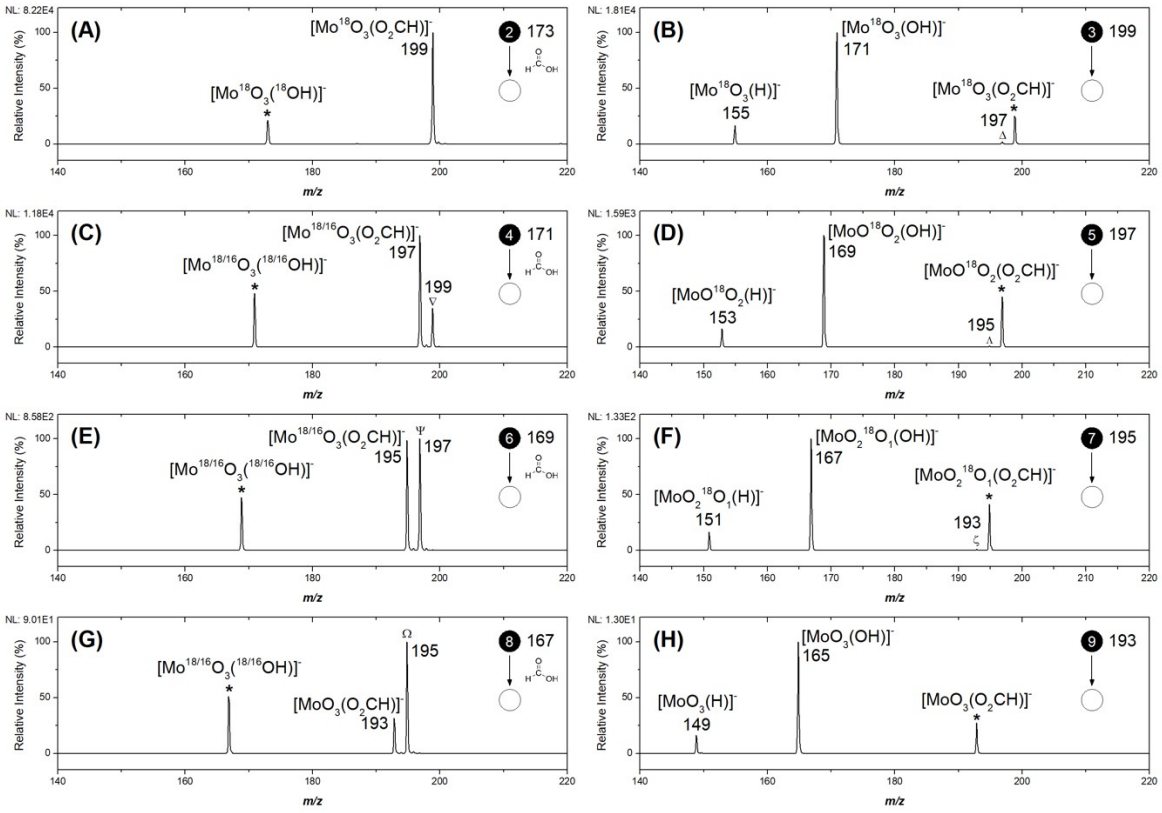

Fig. S11 Multistage mass spectrometry (MS^n) experiments on ^{18}O-labelled molybdate anions. Ion-molecule reactions (IMR) of $[^{100}Mo^{18/16}O_3(^{18/16}OH)]^-$ with HCO_2H were obtained at the given activation times, collision-induced dissociation (CID) experiments on $[^{100}Mo^{18/16}O_3(O_2CH)]^-$ were obtained using a Q value of 0.25 and an activation time of 10 ms with the given Normalised Collision Energies (NCE): (A) MS^2 IMR on $[^{100}Mo^{18}O_3(^{18}OH)]^-$ (*m/z* 173) at 500 ms; (B) MS^3 CID of $[^{100}Mo^{18}O_3(O_2CH)]^-$ (*m/z* 199) (NCE = 16%). (Δ) denotes a secondary product ion corresponding to $[^{100}MoO^{18}O_2(O_2CH)]^-$ (*m/z* 197); (C) MS^4 IMR on $^{18}O/^{16}O$ scrambled $[^{100}Mo^{18/16}O_3(^{18/16}OH)]^-$ (*m/z* 171) at 400 ms. (Λ) corresponds to $[^{100}Mo^{18}O_3(O_2CH)]^-$ (*m/z* 199); (D) MS^5 CID of $[^{100}MoO^{18}O_2(O_2CH)]^-$ (*m/z* 197) (NCE = 15%). (Λ) denotes a secondary product ion corresponding to $[^{100}MoO_2{}^{18}O_1(O_2CH)]^-$ (*m/z* 195); (E) MS^6 IMR on $[^{100}Mo^{18/16}O_3(^{18/16}OH)]^-$ (*m/z* 169) at 500 ms. (ψ) corresponds to $[^{100}MoO^{18}O_2(O_2CH)]^-$ (*m/z* 197); (F) MS^7 CID of $[^{100}MoO_2{}^{18}O_1(O_2CH)]^-$ (*m/z* 195) (NCE = 15%). (ζ) denotes a secondary product ion corresponding to $[^{100}MoO_3(O_2CH)]^-$ (*m/z* 193); (G) MS^7 IMR on $[^{100}Mo^{18/16}O_3(^{18/16}OH)]^-$ (*m/z* 167) at 400 ms. (Ω) corresponds to $[^{100}MoO_2{}^{18}O_1(O_2CH)]^-$ (*m/z* 195); (H) MS^9 CID of $[^{100}MoO_3(O_2CH)]^-$ (*m/z* 193) (NCE = 16%). An asterisk (*) denotes the mass selected precursor ion.

Equations associated with sequential $^{18}O/^{16}O$ scrambling found in Fig. S11.

Fig. S11D:

$[^{100}MoO^{18}O_2(O_2CH)]^-$ → $[^{100}MoO^{18}O_2(OH)]^-$ + CO (S1)
2(¹⁸O₂), *m/z* 197 **1(¹⁸O₂)**, *m/z* 169

$[^{100}MoO^{18}O_2(O_2CH)]^-$ → $[^{100}Mo^{18}O_3(H)]^-$ + CO_2 (S2)
2(¹⁸O₂), *m/z* 197 **3(¹⁸O₂)**, *m/z* 153

Fig. S11E:

$[^{100}MoO^{18}O_2(OH)]^-$ + HCO_2H → $[^{100}MoO^{18}O_2(O_2CH)]^-$ + H_2O (S3a)
1(¹⁸O₂), *m/z* 169 **2(¹⁸O₂)**, *m/z* 197

$[^{100}MoO_2{}^{18}O(^{18}OH)]^-$ + HCO_2H → $[^{100}MoO_2{}^{18}O(O_2CH)]^-$ + $H_2{}^{18}O$ (S3b)
1(¹⁸O₂)', *m/z* 169 **2(¹⁸O₁)**, *m/z* 195

Fig. S11F:

$[^{100}MoO_2{}^{18}O(O_2CH)]^-$ → $[^{100}MoO^{18}O_2(OH)]^-$ + CO (S4)
2(¹⁸O₁), *m/z* 195 **1(¹⁸O₁)**, *m/z* 167

$[^{100}MoO_2{}^{18}O(O_2CH)]^-$ → $[^{100}MoO_2{}^{18}O(H)]^-$ + CO_2 (S5)
2(¹⁸O₁), *m/z* 195 **3(¹⁸O₁)**, *m/z* 151

Fig. S11G:

$[^{100}MoO_2{}^{18}O(OH)]^-$ + HCO_2H → $[^{100}MoO_2{}^{18}O(O_2CH)]^-$ + H_2O (S6a)
1(¹⁸O₁), *m/z* 167 **2(¹⁸O₁)**, *m/z* 195

$[^{100}MoO_3(^{18}OH)]^-$ + HCO_2H → $[^{100}MoO_3(O_2CH)]^-$ + $H_2{}^{18}O$
1(¹⁸O₁)', *m/z* 167 **2**, *m/z* 193 (S6b)

Fig. S11H: (note: same as eqs 5 and 6, but with different Mo isotope).

$[^{100}MoO_3(O_2CH)]^-$ → $[^{100}MoO_3(OH)]^-$ + CO (S7)
2, *m/z* 193 **1**, *m/z* 165

$[^{100}MoO_3(O_2CH)]^-$ → $[^{100}MoO_3(H)]^-$ + CO_2 (S8)
2, *m/z* 193 **3**, *m/z* 149

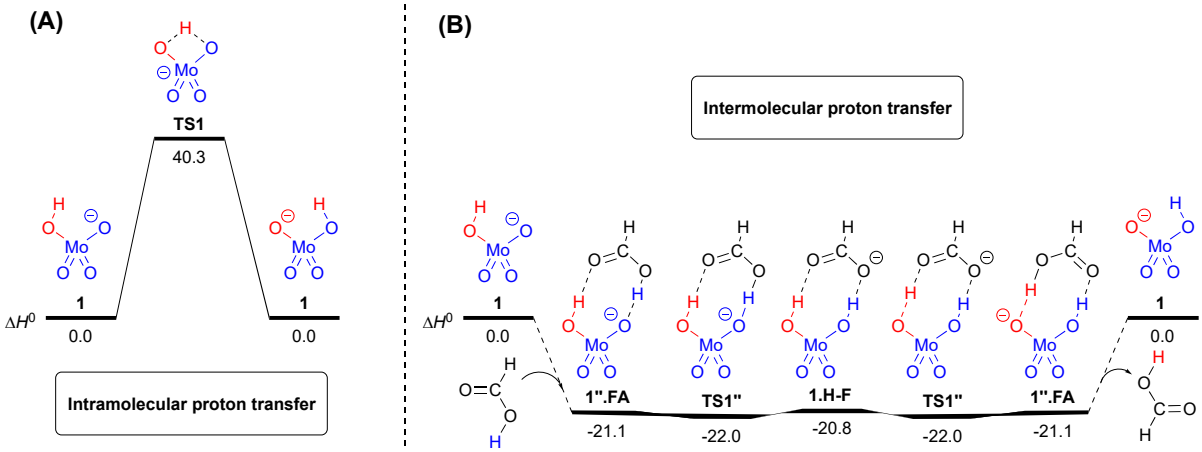

Fig. S12 DFT calculated energy diagrams relevant to the $^{18}O/^{16}O$ scrambling pathways: (A) intramolecular proton transfer pathway (eq. 17); (B) intermolecular proton transfer pathway (eq. 18). The relative enthalpies (ΔH^0 (0 K) are given in kcal mol^{-1} and are calculated at the ωB97M-D3(BJ)/def2-QZVPP//ωB97XD/def2-TZVP level of theory.

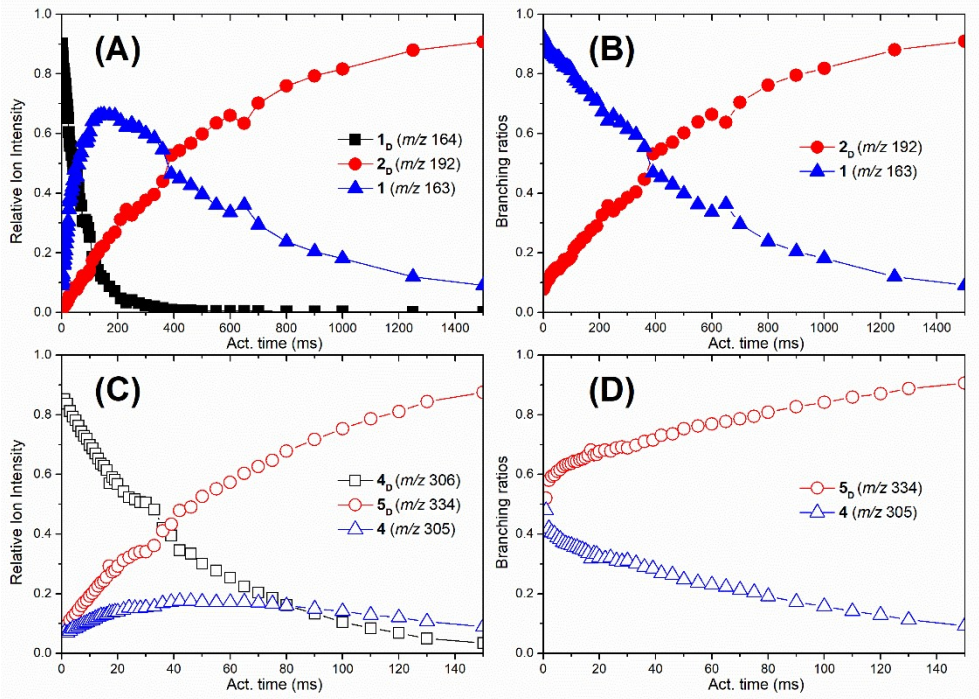

Fig. S13 Kinetic plots for the multistage mass spectrometry ion-molecule reaction experiments (MS^n IMR) on $[(MoO_3)_x(OD)]^-$ (x = 1 – 2) with d_1-formic acid (DCO_2H) ($[DCO_2H]$ ion trap = 3.6 × 10^{10} molecule cm^{-3}). (A) Kinetic curve for the MS^4 IMR of $[MoO_3(OD)]^-$ (**1$_D$**, *m/z* 164) showing depletion of **1$_D$** (black squares, closed) and product ion formation *via* dehydration (**2$_D$**, red circles, closed) and H/D exchange (**1**, blue triangles, closed); (B) Normalised branching ratios for the product ions **2$_D$** and **1** observed in (A); (C) Kinetic curve for the MS^5 IMR of $[Mo_2O_6(OD)]^-$ (**4$_D$**, *m/z* 306) showing depletion of **4$_D$** (black squares, open) and product ion formation *via* dehydration (**5$_D$**, red circles, open) and H/D exchange (**4**, blue triangles, open); (D) Normalised branching ratios for the product ions **5$_D$** and **4** observed in (C). Each point represents the intensity of the ion peaks as a proportion of the total product ion intensity at various activation times (ms).

Table S2: Benchmarking of various levels of theory to best reproduce the energies for decomposition of formic acid *via* dehydrogenation (H_2 + CO_2) and decarbonylation (H_2O + CO). Standard heats of formation obtained from NIST Chemistry WebBook. All relative enthalpy (ΔH) values are given in kcal mol^{-1}.

	Dehydrogenation (H_2 + CO_2)	**Decarbonylation (H_2O + CO)**
Standard heats of formation	-3.5	6.3
ωB97XD/def2-TZVPP	-3.4	11.7
ωB97M-D3(BJ)/def2-QZVPP//ωB97XD/def2-TZVPP	-2.8	6.8
PWPB95-D3(BJ)/def2-QZVPP//ωB97XD/def2-TZVPP	-4.9	9.4
DSD-PBEP86-D3(BJ)/def2-QZVPP//ωB97XD/def2-TZVPP	-4.3	9.3

Discussion on alternative mechanisms for reaction (4) involving protonation of an oxo ligand.

Proton transfer from formic acid to the oxo- ligand of $[MoO_3(OH)]^-$, **1**, proceeds *via* **TS1-15a** (Fig. S14). Following the imaginary mode in one direction gives the five-coordinate complex $[(HCO_2)Mo(O)_2(OH)_2]^-$, **15a**, where the formate, HCO_2^-, is bound to the Mo(VI) center. Following the imaginary mode in the other direction shows the formation of an initial ion-molecule complex, **1.FA'**, where the acidic proton of formic acid is hydrogen bonding to the oxo- ligand to be protonated. We have not been able to optimize the structure of **1.FA'** as an energy minimum however linear potential energy surface (PES) scans (Fig. S16) indicate its formation as formic acid, HCO_2H, and $[MoO_3(OH)]^-$, **1**, come together in an ion-molecule reaction. The estimated activation barrier for the proton transfer in **TS1-15a** is $\Delta H^{0‡}$ +7.5 kcal mol^{-1}. Compared to protonation of the hydroxo- ligand (Fig. 5), a similar activation barrier is observed for **TS1-2** of $\Delta H^{0‡}$ +7.7 kcal mol^{-1}. However, we note that the overall ΔH^0 of **TS1-15a** (-12.2 kcal mol^{-1}) is lower than that of **TS1-2** (-8.2 kcal mol^{-1}).

Upon formation of the five-coordinate $[(HCO_2)Mo(O)_2(OH)_2]^-$, **15a**, elimination of water can proceed *via* several similar pathways to give $[MoO_3(O_2CH)]^-$, **2**, as observed in the MS-IMR experiments. These pathways are summarized in Fig. S14-S15 and described briefly here.

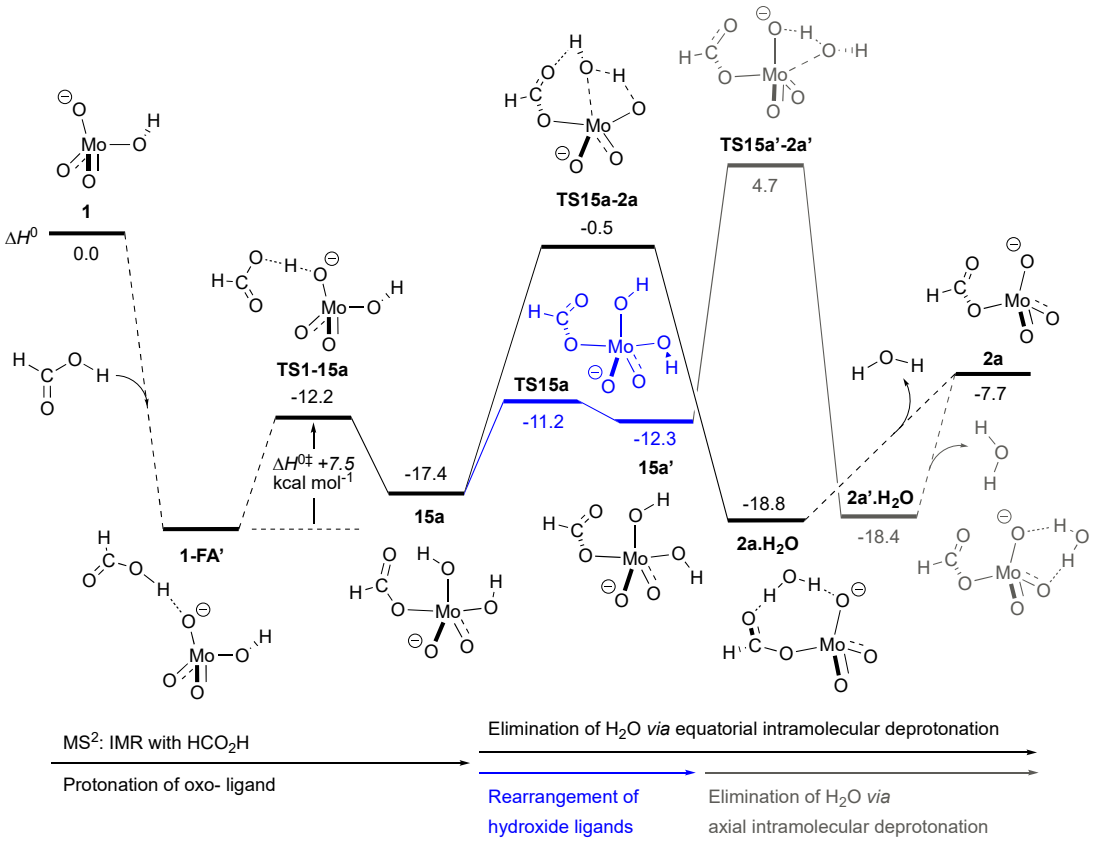

Fig. S14 DFT calculated energy surface for the ion-molecule reaction of $[MoO_3(OH)]^-$ with HCO_2H. Protonation at an oxo- ligand followed by the elimination of water *via* intramolecular deprotonation. Elimination of water from equatorial position (black). Rearrangement of hydroxide ligands (blue) followed by elimination of water from axial position (gray). The relative enthalpies ΔH^0 (0 K) are given in kcal mol^{-1} and are calculated at the ωB97M-D3(BJ)/def2-QZVPP//ωB97XD/def2-TZVPP level of theory.

The most energetically favorable pathway found occurs through an equatorial displacement of H_2O from **15a** through **TS15a-2a** (ΔH^0 = -0.5 kcal mol^{-1}). Deprotonation of the hydroxide in the axial position of **15a** and attack of the equatorial hydroxide **TS15a-12a** ($\Delta H^{0‡}$ = +16.9 kcal mol^{-1}) results in the formation of H_2O in the hydrogen bonded ion-molecule complex $[MoO_3(O_2CH).H_2O]^-$, **2a.H$_2$O**, akin to what was observed in Fig. 5. Removal of H_2O results in **2a**. Alternatively, the hydroxide ligands in **15a** can undergo a rearrangement *via* **TS15a** to give **15a'** where the hydroxide ligands are set up to undergo water elimination from an axial position (**TS15a'-2a'**). This gives the ion-molecule complex **2a'.H$_2$O** which is an isomer of **2a.H$_2$O** where the H_2O is bound to **2a** in a different position. We note that the difference in energies between **2a.H$_2$O** and **2a'.H$_2$O** are minor. The key transition state barrier for this channel is *ca.* 5.2 kcal mol^{-1} higher in energy than elimination of H_2O *via* equatorial intramolecular deprotonation.

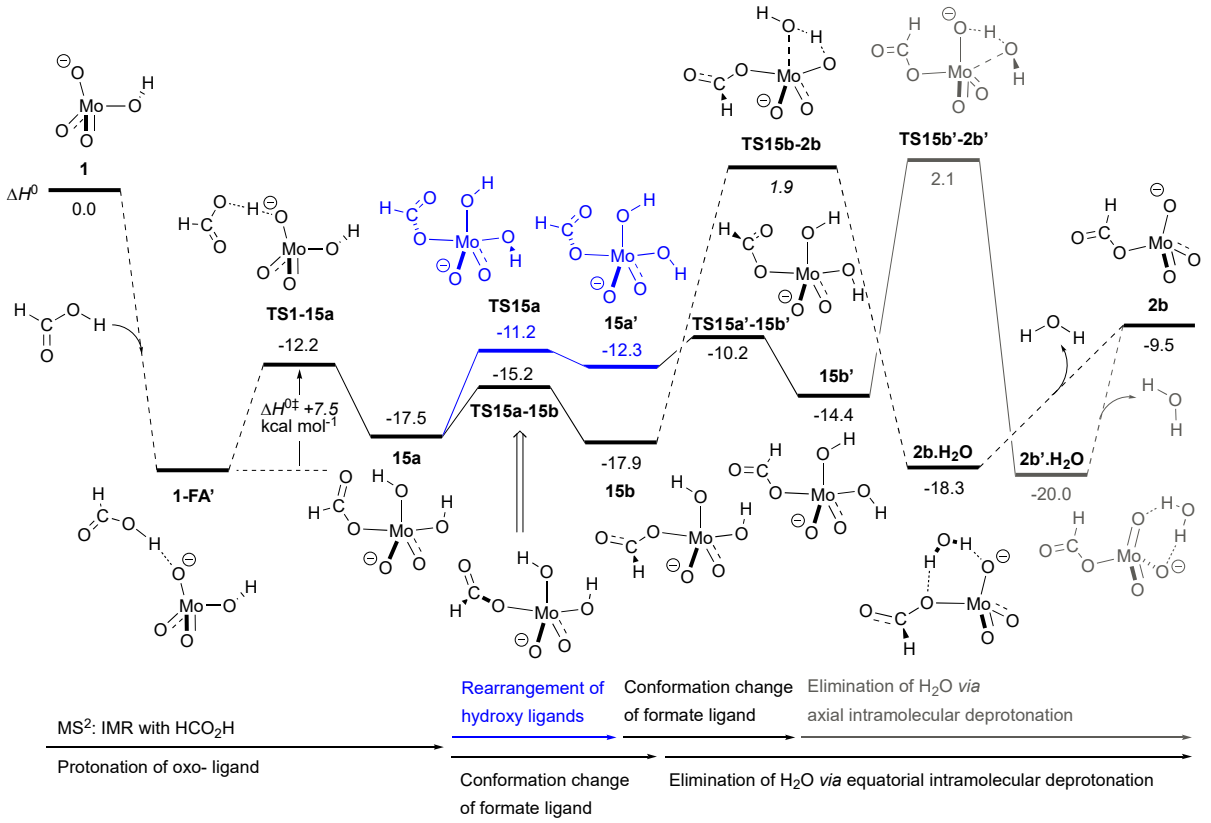

Fig. S15 DFT calculated energy surface for the ion-molecule reaction of $[MoO_3(OH)]^-$ with HCO_2H. Protonation at an oxo- ligand followed by the elimination of water *via* intramolecular deprotonation. The relative enthalpies ΔH^0 (0 K) are given in kcal mol^{-1} and are calculated at the ωB97M-D3(BJ)/def2-QZVPP//ωB97XD/def2-TZVPP level of theory.

Fig. S15 summarizes several pathways possible for the elimination of water *via* intramolecular deprotonation to give the conformer $[MoO_3(O_2CH)]^-$, **2b**. These pathways mirror those presented in Fig. S14 and as such will be discussed in lesser detail. However, all appear to connect to **15a** as a key intermediate that is initially formed in the IMR with HCO_2H. A conformation change of the formate ligand *via* **TS15a-15b** ($\Delta H^{0‡}$ = +2.2 kcal mol^{-1}) gives **15b** where the C1-proton of the formate ligand is now hydrogen bonded to one of the oxo- ligands. Elimination water from the equatorial position *via* intramolecular deprotonation occurs through **TS15b-2b** to give **2b.H$_2$O**. We have not been able to locate an optimized structure for **TS15b-2b** and have estimated the relative ΔH^0 based on the linear PES scan shown below (Fig. S17). Removal of H_2O from **2b.H$_2$O** gives **2b**. Alternatively, the hydroxide ligands in **15a** can undergo a rearrangement first, *via* **TS15a** to give **15a'**, prior to the conformational change of the formate ligand resulting in **15b'** where now the C1-proton of the formate ligand is hydrogen bonding to one of the hydroxo- ligands. Water is then eliminated from the axial position of **15b'** to give **2b'.H$_2$O**.

Whilst the key transition states found for the elimination of water only differ by a few kcal mol^{-1}, only the pathway found occurring through **TS15a-2a** is below the 'zero' energy. Moreover, this remains greater than the key transition state barrier **TS1-2** observed in Fig. 5 for protonation of the coordinated hydroxide by formic acid and elimination of H_2O . So while the initial protonation of an oxo-ligand may be lower in energy, the subsequent rearrangements required prior to elimination from **15a** presents a significant barriers.

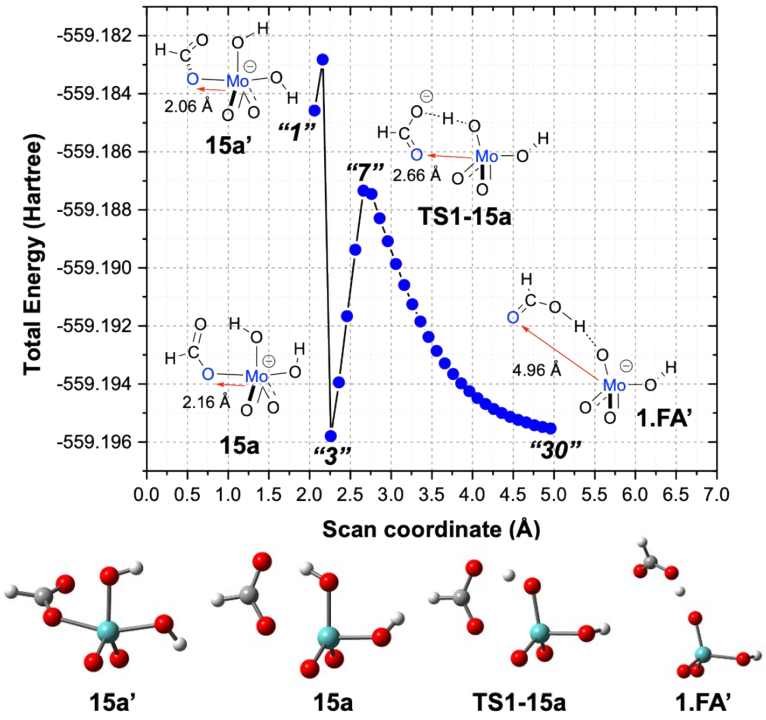

Fig. S16 Linear potential energy surface (PES) scan along Mo-O bond (increasing). Structure "*1*" corresponds to **15a'** (Fig. S14); Structure "*3*" corresponds to **15a** (Fig. S14); Structure "*7*" corresponds to **TS1-15a** (Fig. S14); Structure "*30*" corresponds to **1.FA'** (Fig. S14).

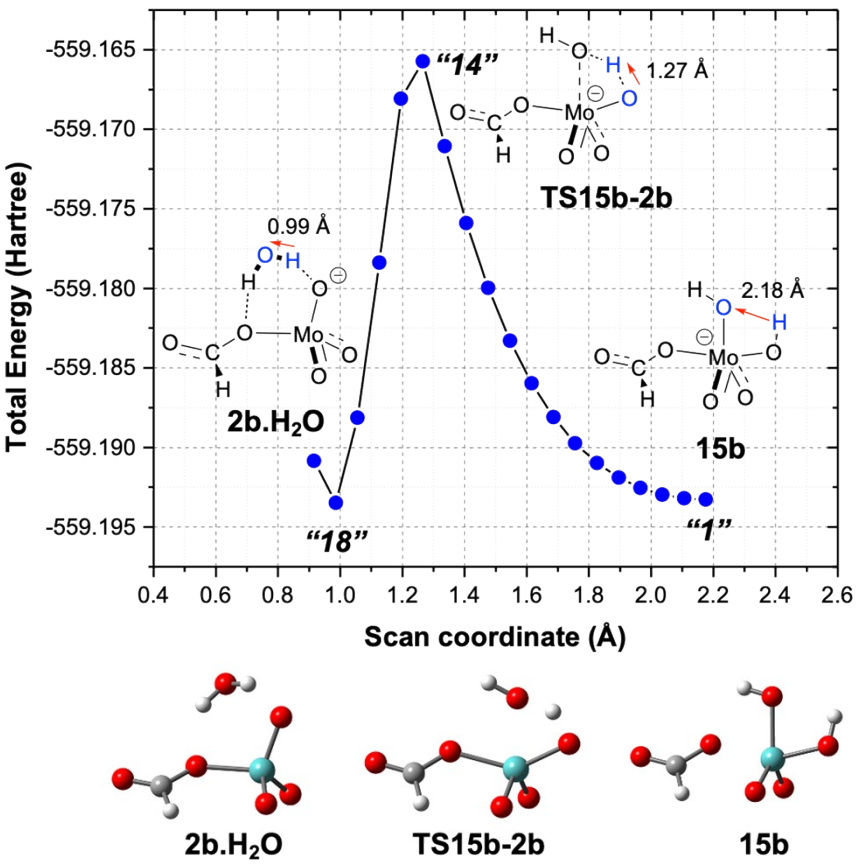

Fig. S17 Linear potential energy surface (PES) scan along O-H bond (decreasing) showing the elimination of water from equatorial intramolecular deprotonation to give **2b.H_2O** (Fig. S15). Structure "*1*" corresponds to **15b** (Fig. S15); Structure "*14*" corresponds to **TS15b-2b** (Fig. S15); Structure "*18*" corresponds to **2b.H_2O** (Fig. S15).

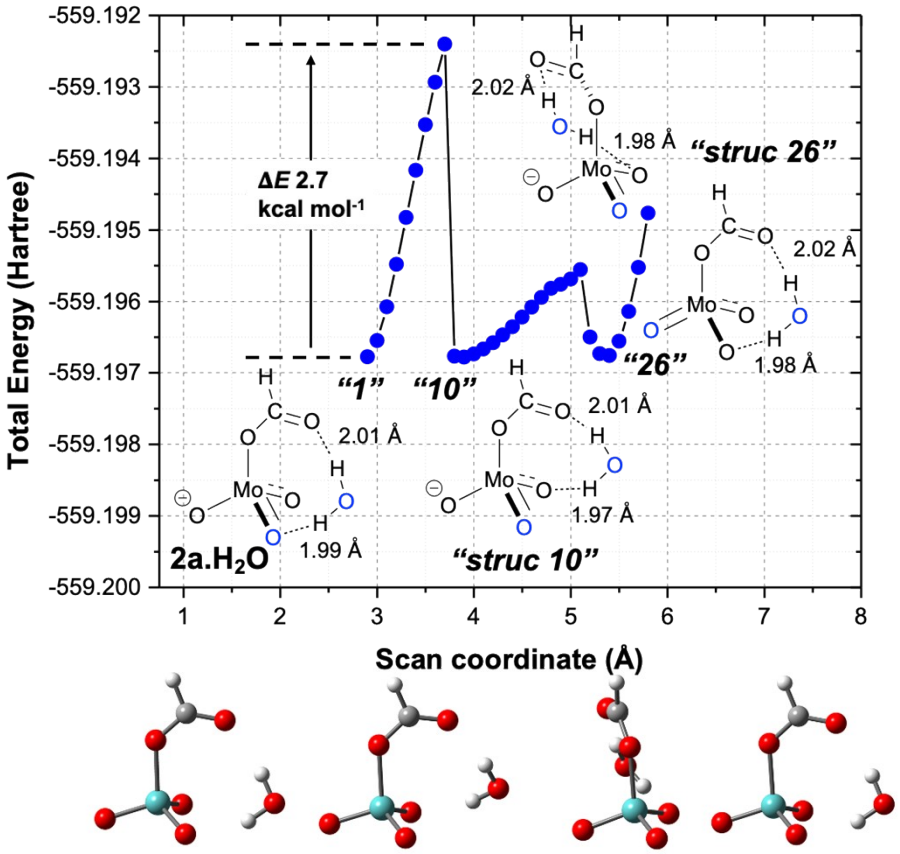

Fig. S18 Linear potential energy surface (PES) scan along O-O bond (increasing). Structure "*1*" corresponds to **2a.H_2O** (Fig. 5 and S14).

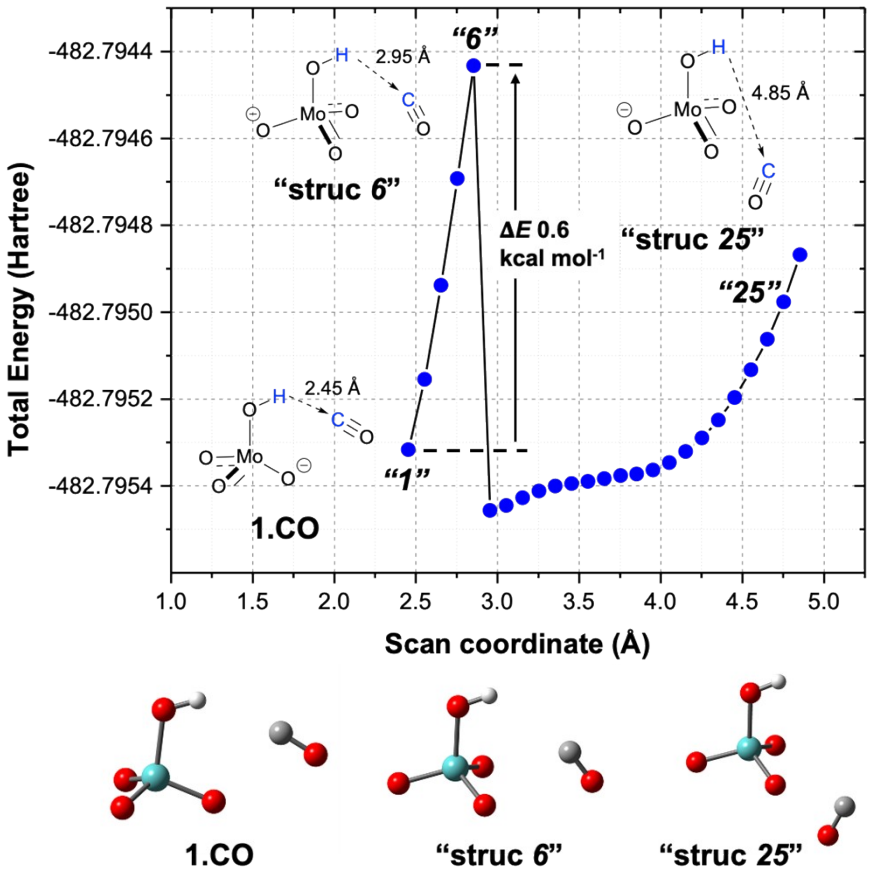

Fig. S19 Linear potential energy surface (PES) scan along H-C bond (increasing). Structure "*1*" corresponds to **1.CO** (Fig. 5).

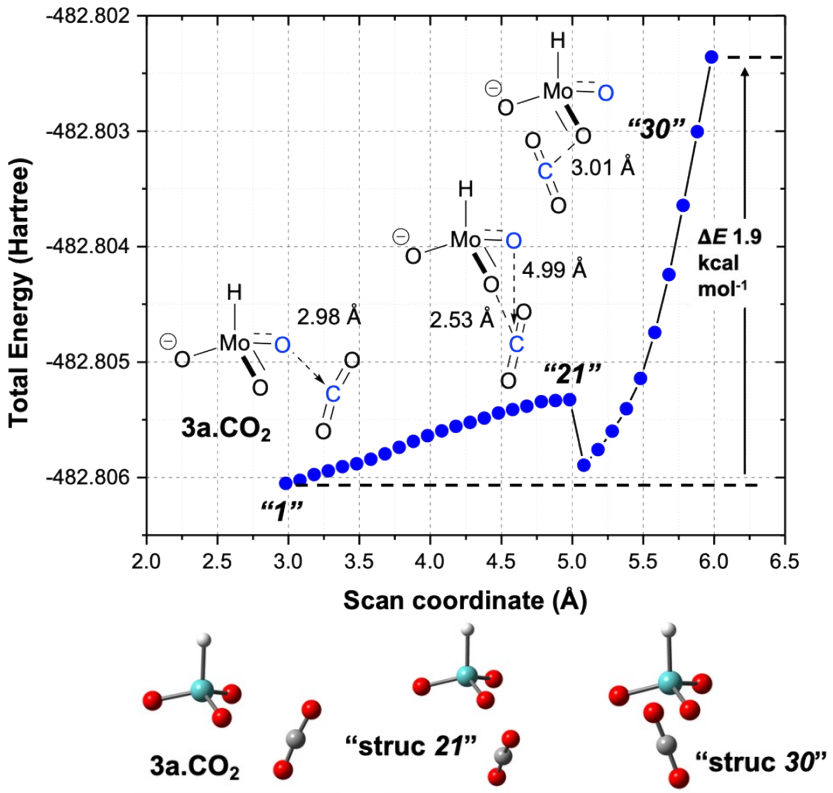

Fig. S20 Linear potential energy surface (PES) scan along O-C bond (increasing). Structure "*1*" corresponds to **3a.CO$_2$** (Fig. 5).

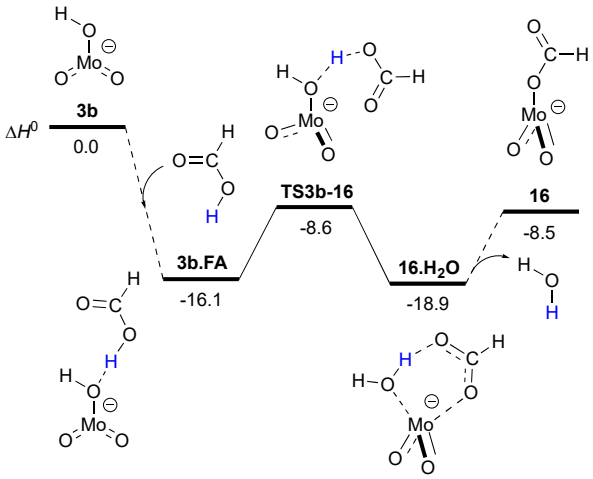

Fig. S21 DFT calculated energy surface for the reaction between [MoO$_2$(OH)]$^-$, **3b**, and HCO$_2$H. The relative enthalpies (ΔH^0 (0 K) are given in kcal mol^{-1} and are calculated at the ωB97M-D3(BJ)/def2-QZVPP//ωB97XD/def2-TZVP level of theory.

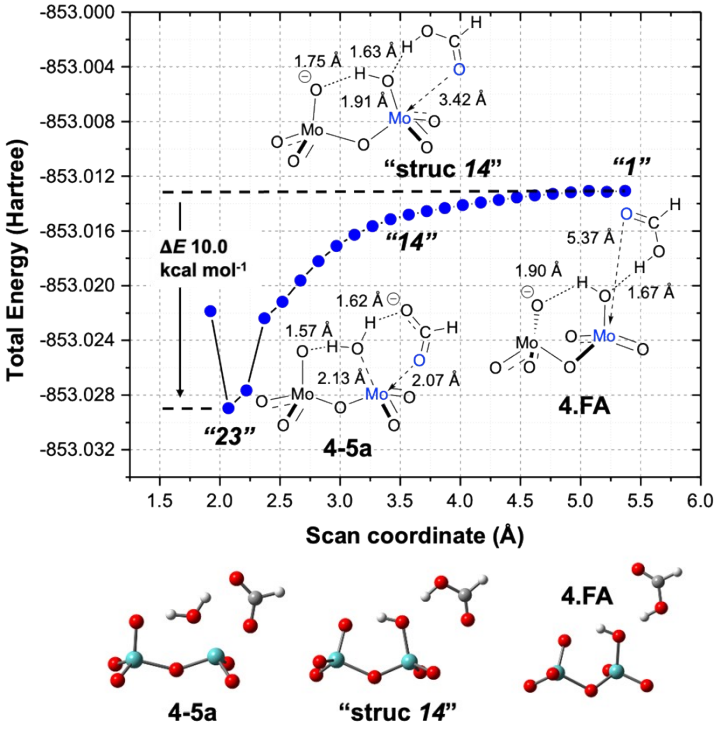

Fig. S22 Linear potential energy surface (PES) scan along the O(formate)-Mo bond (decreasing). Structure "*1*" corresponds to **4.FA** (Fig. 6); Structure "*23*" corresponds to **4-5a** (Fig. 6).

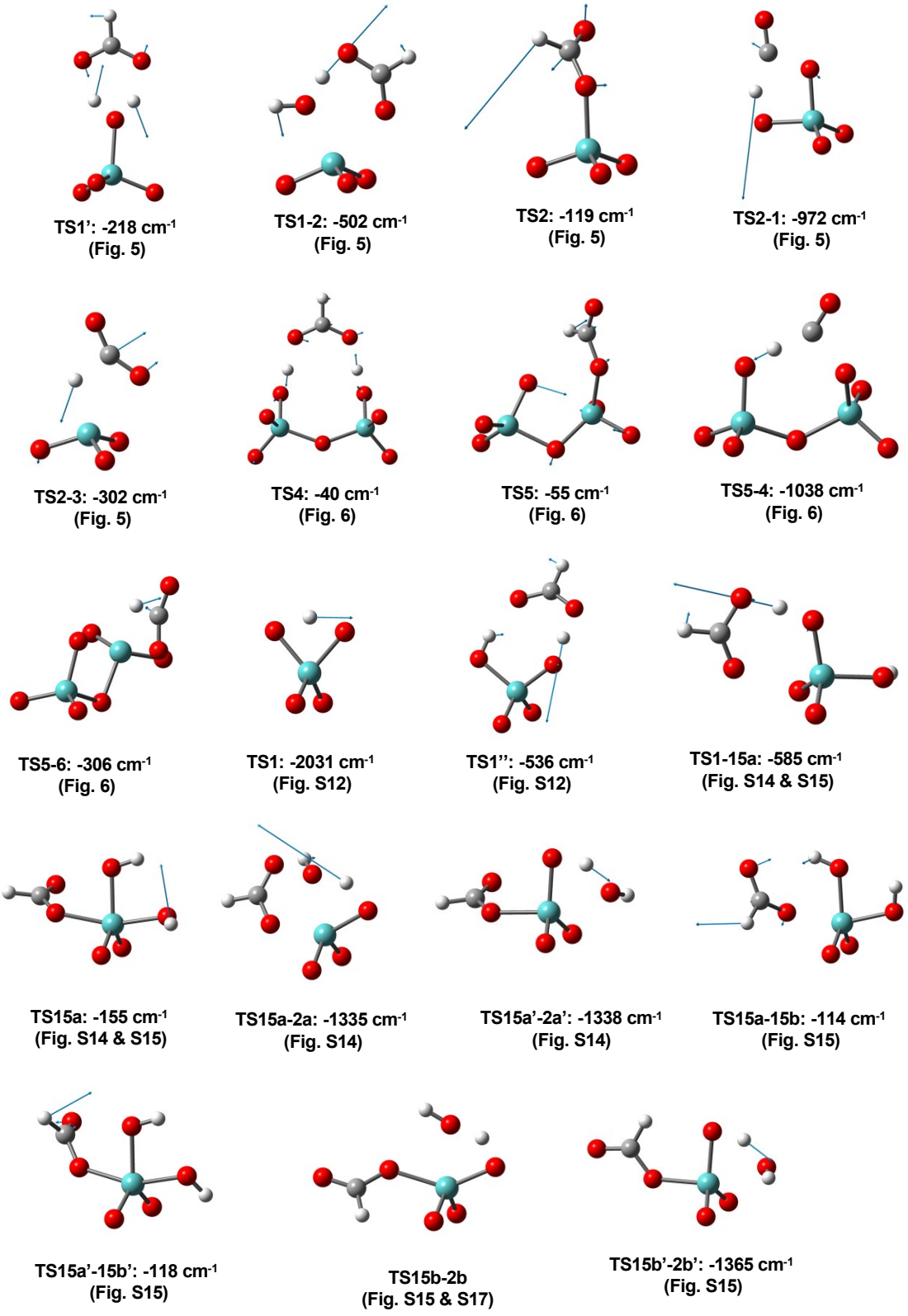

Fig. S23 Structures of transition states showing vectors associated with imaginary frequencies. Cartesian coordinates for each structure can be found in the associated xyz file.

Example of DSD-PBEP86-D3(BJ) input for ORCA5.0.3

```
*xyzfile 0 1 struc.xyz
! B2PLYP D3BJ RIJK def2-QZVPP def2-QZVPP/C def2/JK TIGHTSCF PAL8
%method
FrozenCore FC_ELECTRONS
Exchange x_PBE
Correlation c_P86
LDAOpt C_VWN5
ScalHFX 0.69
ScalDFX 0.31
ScalGGAC 0.44
ScalLDAC 0.44
ScalMP2C 1.00
end
%method
D3S6 0.48
D3A1 0.0
D3S8 0.0
D3A2 5.6
end
%mp2
RI on
DoSCS True
Ps 0.52
Pt 0.22
end
```

Example of PWPB95-D3(BJ) input for ORCA5.0.3

```
! RIJK RI-PWPB95 D3BJ def2-QZVPP def2/JK def2-QZVPP/C TIGHTSCF PAL4
*xyzfile 0 1 struc.xyz
```

References

1. G. Sheldrick, *Acta Crystallogr. Section C*, **2015**, **71**, 3-8.

2. C.F. Macrae, I.J. Bruno, J.A. Chisholm, P.R. Edgington, P. McCabe, E. Pidcock, L. Rodriguez-Monge, R. Taylor, J. van de Streek, P.A. Wood, *J. Appl. Cryst*. **2008**, *41*, 466–470.

3. Farrugia, L. J.; *J. Appl. Cryst.* **1999**, *32*, 837-838.